Optimality in Self-Organized Molecular Sorting

Optimality in self-organized molecular sorting

Marco Zamparo,[1,2,*] Donatella Valdembri,[3,4,*] Guido Serini,[3,4,†] Igor V. Kolokolov,[5,6,‡] Vladimir V. Lebedev,[5,6,§] Luca Dall'Asta,[1,7,8,2,¶] and Andrea Gamba[1,2,8,**]

[1] *Institute of Condensed Matter Physics and Complex Systems, Department of Applied Science and Technology, Politecnico di Torino, Corso Duca degli Abruzzi 24, 10129 Torino, Italy*
[2] *Italian Institute for Genomic Medicine c/o Candiolo Cancer Institute, Fondazione del Piemonte per l'Oncologia (FPO), Istituto di Ricovero e Cura a Carattere Scientifico (IRCCS), Candiolo, 10060 Torino, Italy*
[3] *Department of Oncology, University of Torino School of Medicine, Candiolo, 10060 Torino, Italy*
[4] *Candiolo Cancer Institute, Fondazione del Piemonte per l'Oncologia (FPO), Istituto di Ricovero e Cura a Carattere Scientifico (IRCCS), Candiolo, 10060 Torino, Italy*
[5] *L.D. Landau Institute for Theoretical Physics, 142432, Moscow Region, Chernogolovka, Ak. Semenova, 1-A, Russia*
[6] *National Research University Higher School of Economics, 101000, Myasnitskaya 20, Moscow, Russia*
[7] *Collegio Carlo Alberto, Via Real Collegio 30, 10024 Moncalieri, Italy*
[8] *Istituto Nazionale di Fisica Nucleare (INFN), Italy*

We introduce a simple physical picture to explain the process of molecular sorting, whereby specific proteins are concentrated and distilled into submicrometric lipid vesicles in eukaryotic cells. To this purpose, we formulate a model based on the coupling of spontaneous molecular aggregation with vesicle nucleation. Its implications are studied by means of a phenomenological theory describing the diffusion of molecules towards multiple sorting centers that grow due to molecule absorption and are extracted when they reach a sufficiently large size. The predictions of the theory are compared with numerical simulations of a lattice-gas realization of the model and with experimental observations. The efficiency of the distillation process is found to be optimal for intermediate aggregation rates, where the density of sorted molecules is minimal and the process obeys simple scaling laws. Quantitative measures of endocytic sorting performed in primary endothelial cells are compatible with the hypothesis that these optimal conditions are realized in living cells.

Keywords: protein sorting, phase separation, self-organization, physical kinetics, scaling laws, lattice gas

Introduction To counter the homogenizing effect of diffusion, eukaryotic cells developed an elaborate system to sort and distill specific proteins into submicrometric lipid vesicles, that are then transported towards appropriate intracellular destinations by active mechanisms involving molecular motors [1, 2]. Molecule sorting takes place on the plasma membrane, on inner membrane bodies (endosomes) and in the Golgi membrane network. Common biochemical principles involving the action of specialized proteins that promote membrane bending and fission [3–7] underlie molecular sorting in these different locations [1, 2, 8]. But can molecular sorting be understood as a sistemic process, beyond the molecular detail? Self-aggregation processes driven by reinforcing feedback loops lead to the formation of submicrometric domains enriched in specific lipids and proteins, and are ubiquitous on cell membranes [see Refs. 9–11, and references therein]. Moreover, the formation of such molecular aggregates, which can be likened to a phase separation process, that, along with sorted cargo, may involve several adaptor, membrane-bending and fission-inducing proteins, has been observed to precede and induce vesicle nucleation [12, 13], and evidences suggest that protein crowding by itself can drive membrane bending and vesicle nucleation [14–19] by making these processes energetically favorable [20–25]. Altogether, these observations suggest that sorting may be a universal process emerging from the coupling of two main components: a) the self-aggregation of localized protein microdomains, and b) vesicle nucleation. In this scheme, molecules that diffuse on a membrane can aggregate into localized enriched domains that grow due to molecule absorption. When a domain reaches a sufficiently large size, its biochemical constituents locally induce higher membrane curvature and the consequent nucleation and detachment of a small vesicle. The newly generated vesicle is constitutively enriched in the biochemical factors of the engulfed domain, resulting in a spontaneous distillation process. Here, we formulate a phenomenological theory of molecular sorting based on these principles and compare its predictions with numerical simulations of a lattice-gas model and quantitative measures of the kinetics of endocytic sorting in living cells. Our analysis suggests that higher sorting efficiency is realized when the number of sorting domains is minimized, a situation taking place for intermediate levels of the self-aggregation strength. Our quantitative measures suggest that such optimal conditions may be realized in living cells.

Phenomenological Theory We describe a situation where molecules arrive on a membrane region, diffuse and aggregate into localized enriched domains, and these domains are removed from the membrane, after reaching

a characteristic size R_E, through the formation of small separate lipid vesicles. In this picture, sorting domains coexist in a statistically stationary state with a continuously repleted dilute solution, or "gas", of molecules that diffuse freely on a membrane. This is reminiscent of two-dimensional diffusion-limited aggregation (DLA) [26] or the related Hele-Shaw problem [27]. However, in the advanced stages of DLA large fractal clusters are formed [26], while in our problem the presence of the cutoff length R_E restricts the domain size, and domain shapes remain approximately round. Here, as in the classical framework of Lifshitz-Slezov (LS) theory [28, 29], domains of size R larger than a critical value R_c grow irreversibly by means of the absorption of single molecules diffusing towards them. This mechanism is expected to provide the dominant contribution to the absorption dynamics for sufficiently small average molecule density $\bar{n}$ in the gas. For domains with sizes much larger than the critical size R_c, the density n_0 near the domain boundary is independent of its size. When the typical inter-domain distance L is much larger than R_E, the difference Δn in molecule density between the regions farther away and closer to the domain boundaries is approximately given by $\bar{n} - n_0 > 0$. Contrary to LS theory, in which domains can grow arbitrarily in time and Δn tends to zero as time grows, here the size of domains removed from the system introduces a cutoff length $R_E \gg R_c$, and, in the statistically stationary regime, Δn is kept finite by the continuous influx of particles into the system.

The quasi-static profile of the density of freely diffusing molecules in the vicinity of a circular domain of size R is obtained solving the Laplace equation with Dirichlet boundary conditions:

$$n(r) = n_0 + \frac{\ln r/R}{\ln L/R}\,\Delta n, \tag{1}$$

where r is the distance from the domain center. Deviations of the domain shape from circularity produce rapidly decaying higher multipole contributions that may be neglected in the main approximation.

The domain grows due to the flux Φ_R of molecules from the gas, which can be found by integrating the flux density $-D\,\nabla n$ over a circle of radius $r \gg R$:

$$\Phi_R = 2\pi R D\,\partial_r n(r)|_{r=R} = \frac{2\pi D \Delta n}{\ln(L/R)}, \tag{2}$$

where D is the diffusion coefficient of isolated molecules. From (2) one obtains the dynamic equation for domain growth, $\dot{R} = A_0 D \Delta n/(R\ln(L/R))$, where A_0 is the area occupied by a molecule in the domain, and the domain size R is such that the domain area is πR^2.

Abstracting from complicated molecular details, the mesoscopic effects of vesicle extraction will be encoded in a single parameter, the rate $\gamma(R)$ by which domains of size R are removed from the system. If $N(t,R)\,\mathrm{d}R$ is the number of domains per unit area with size between R and $R + \mathrm{d}R$, the number density $N(t,R)$ satisfies the Smoluchowski equation

$$\frac{\partial N}{\partial t} + \frac{\partial}{\partial R}(\dot{R}\,N) = -\gamma(R)\,N, \tag{3}$$

A stationary solution of (3) is

$$N_{\mathrm{st}}(R) = \frac{JR\ln(L/R)}{D\Delta n}\exp\left[-\int_0^R \mathrm{d}r\,\frac{r\ln(L/r)\gamma(r)}{A_0 D\Delta n}\right]. \tag{4}$$

We assume that the extraction rate $\gamma(R)$ is negligible for $R < R_E$ and strongly suppresses $N_{\mathrm{st}}(R)$ for $R > R_E$, where R_E is the characteristic size of the domains that are extracted from the membrane. The factor J in Eq. (4) is determined by noticing that, in the stationary regime, the average flux $\int \Phi_R N_{\mathrm{st}}(R)\,\mathrm{d}R$ must equate the incoming flux of molecules per unit area ϕ (one of the control parameters of the theory), thus giving $J \sim \phi/R_E^2$. In the region $R < R_E$ where $\gamma(R)$ is negligible, Eq. (4) shows that the distribution $N_{\mathrm{st}}(R)$ has a universal behavior characterized by a linear growth with logarithmic corrections. The present phenomenological approach is applicable if the inequality $R_E^2 \gg A_0$ is satisfied. This condition also justifies the quasi-static approach leading to Eq. (1).

The efficiency of the sorting process can be measured in terms of the average residence time $\bar{T}$ of a molecule on the membrane system. For absorbing domains, this is the sum of the average time $\bar{T}_{\mathrm{f}}$ required by the molecule to reach a domain by free diffusion and be absorbed, and the average time $\bar{T}_{\mathrm{d}}$ spent inside that domain until the extraction event. For evenly distributed domains, the first contribution $\bar{T}_{\mathrm{f}}$ is inversely proportional to the average number N_{d} of domains per unit area, where $N_{\mathrm{d}} = \int \mathrm{d}R\,N_{\mathrm{st}}(R) \sim \phi/(D\Delta n)$, giving $\bar{T}_{\mathrm{f}} \sim 1/(DN_{\mathrm{d}}) \sim \Delta n/\phi$. In its turn, the average time spent by a molecule in a domain can be estimated as $\bar{T}_{\mathrm{d}} \sim R_E^2/(A_0\Phi_R) \sim R_E^2/(DA_0\Delta n)$, where (2) was used.

The rate of formation of new domains can be estimated as $\mathrm{d}N_{\mathrm{d}}/\mathrm{d}t = CD\bar{n}^2$, where C is a dimensionless quantity characterizing the efficiency of absorption of single molecules by the germ of a domain. In the stationary condition this rate is equal to $N_{\mathrm{d}}/\bar{T}_{\mathrm{d}}$, therefore

$$\bar{n} \sim \left(\frac{\phi A_0}{CDR_E^2}\right)^{1/2}. \tag{5}$$

Assuming $n_0 \lesssim \Delta n$ we get $\Delta n \sim \bar{n}$ and then

$$\bar{T}_{\mathrm{d}} \sim C^{1/2}\frac{R_E^3}{(D\phi)^{1/2}A_0^{3/2}}, \quad \bar{T}_{\mathrm{f}} \sim C^{-1/2}\frac{A_0^{1/2}}{(D\phi)^{1/2}R_E}. \tag{6}$$

The sum $\bar{T} = \bar{T}_{\mathrm{d}} + \bar{T}_f$, as a function of C, has a minimum

in $C \sim A_0^2/R_E^4 \ll 1$, where

$$\bar{T}_{\rm f} \sim \bar{T}_{\rm d} \sim \frac{R_E}{(DA_0)^{1/2}\phi^{1/2}}, \tag{7}$$

$$\bar{n} \sim \Delta n \sim \frac{\phi^{1/2}R_E}{(DA_0)^{1/2}}. \tag{8}$$

Therefore, the scaling relations (7,8) identify the dynamical regime in which molecular sorting is most efficient. The density of molecules accumulated in the domains is

$$\rho_{\rm d} \sim N_{\rm d}R_E^2/A_0 \sim C^{1/2}\frac{\phi^{1/2}R_E^3}{D^{1/2}A_0^{3/2}}. \tag{9}$$

Thus, also the total density $\rho = \bar{n} + \rho_{\rm d}$ has a minimum for $C \sim A_0^2/R_E^4$, and the minimal value of ρ is again determined by the estimate (8).

Lattice-gas model and numerical results To further explore the role of molecule self-aggregation in the distillation process, and to probe the behavior of the sorting process over a wide range of parameter values, we introduce here a minimal lattice-gas model of molecular sorting, without any attempt at a complete description of the complex biochemical and physical details implied in the process of vesicle budding and removal.

We represent the lipid membrane as a two-dimensional square lattice with periodic boundary conditions, where each lattice site can host at most a single molecule [30]. The system evolves according to a Markov process that comprises the following three elementary mechanisms: 1) Molecules from an infinite reservoir arrive and are inserted on empty sites with rate k_I. 2) Then, molecules can perform diffusive jumps to an empty neighboring site with rate $k_D/g^{\#\rm nn}$, where $g > 1$ is a dimensionless aggregation coefficient and #nn is the number of molecules neighboring the site originally occupied by the jumping molecule. 3) Finally, molecules are extracted from the system by the simultaneous removal of all connected molecule clusters, if any, that contain a completely filled square of linear size ℓ, with $\ell^2 \sim R_E^2/A_0$ (for a formal mathematical definition see SM). The stationary properties of the model depend on only two parameters, the ratio k_I/k_D and the aggregation coefficient g. In what follows, areas are measured in units of a lattice site, therefore $A_0 = 1$, and the particle densities ρ, n are dimensionless quantities.

The statistically stationary state of the model was investigated numerically. Fig. 1(a) shows that the stationary density of molecules ρ is low for intermediate values of g, where a dilute gas of free molecules coexists with growing domains. In this region, the fraction of free molecules decreases as g is increased, and the total molecule density has a minimum. The neighborhood of this minimum corresponds to the region previously found from the analysis of the phenomenological theory, which is likely the most interesting from the biological point of view. In Fig. 1(b) the total density ρ is decomposed into the contributions of freely diffusing molecules and of the molecules which are part of sorting domains. When g is increased, the density of freely diffusing molecules decreases, while the number of molecules in the domains increases, leading to the appearance of a minimum of ρ (Fig. 1(b), white circles) at intermediate values of the aggregation coefficient g. In this region, we computed numerical scaling relations with respect to the incoming flux per unit site $\phi = k_I(1-\rho)$, finding good agreement with the theoretical predictions (7–9) (Fig. 1(c)–(d) and figure legend).

To characterize the efficiency of the sorting process we computed numerically the sorting rate $\bar{T}^{-1} = \phi/\rho$ (see SM and Ref. [31]) in terms of the physically meaningful parameters ϕ and g [32]. Fig. 1(e) shows that $\bar{T}^{-1}$ increases monotonically with ϕ, and that it exhibits a maximum as a function of g at fixed ϕ (the dashed line in Fig. 1(e) marks the position of these maxima). In the optimal sorting region located around the maxima of $\bar{T}^{-1}$ distillation of molecular factors is most efficient.

The numerical evidence of a region of optimal sorting is in agreement with the phenomenological theory. This can be seen by considering that, in the framework of the numerical scheme, the efficiency C of absorption of single molecules increases monotonically with g. Then the existence of the maximum of the sorting rate $\bar{T}^{-1}$ and of the minimum of the density ρ observed in the numerical modeling appears as a natural consequence of the phenomenological theory. The contrasting behavior of the density of particles in the gas and in the domains (Fig. 1(b)) agrees with Eqs. (5,9).

Along with the residence time $\bar{T}$, which is a property of the stationary state, we considered also the characteristic adaptation time $T_{\rm ad}$ needed by the membrane system to approach the stationary state after the sudden onset of a nonzero external stimulus. Numerical simulations show that $T_{\rm ad}$ is directly correlated to $\bar{T}$ (see SM). Therefore, parameter values that correspond to optimal sorting in the stationary state are also those that provide faster response to changing environmental signals.

Comparison with experimental data It is interesting to check how experimental data compare with our general physical theory. Low-density lipoproteins (LDL) bind to LDL receptors (LDLR) on the plasma membrane in a 1:1 ratio, diffuse laterally, aggregate and are internalized in endocytic vesicles (see Refs. 33, 1 and SM). They provide a convenient experimental system whose behavior can be compared with the theory. We performed experiments of endocytic sorting of LDL on primary human endothelial cells incubated with LDL particles for 1 hour prior to imaging to allow them to reach a stationary state (see [34] and SM for details). LDL particles tagged with Alexa Fluor 488 green fluorescent dye were employed (SM). The local density of fluorescently-tagged molecules was quantified using total internal reflection fluorescence (TIRF) microscopy (Fig. 2(a)), which allows to constrain the

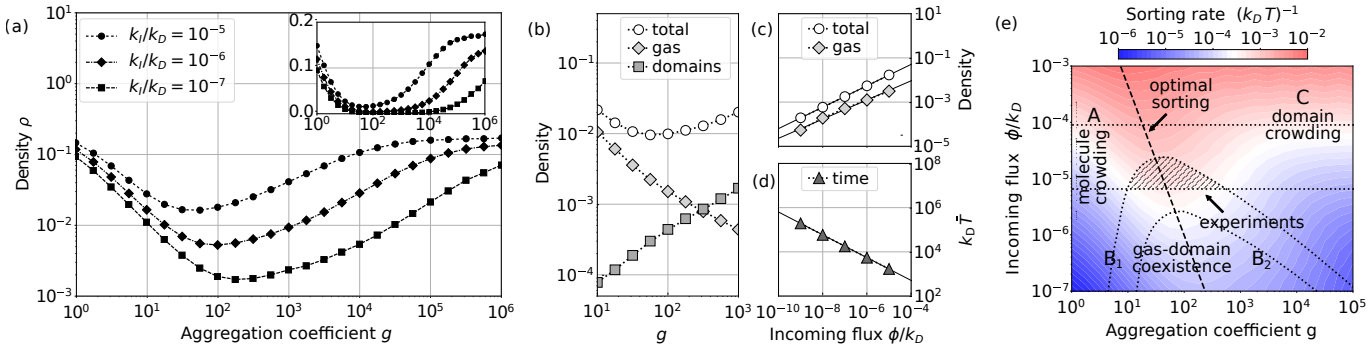

Figure 1. (a) Molecule density ρ (time average in the statistically stationary state) as a function of the aggregation coefficient g, for $k_I/k_D = 10^{-5}, 10^{-6}, 10^{-7}$. Inset: same quantities in log-linear scale. (b) Partial molecule densities as functions of the aggregation coefficient g. The density of the gas component decreases, while the number of molecules in the interior of sorting domains increases for growing g at fixed $\phi/k_D = 10^{-8}$; as a consequence, the total molecule density has a minimum at an intermediate value of g. (c,d) Numerical evidence of scaling relations. Straight lines are fitted with the laws $\rho \sim \phi^a$, $\bar{n} \sim \phi^b$, and $\bar{T} \sim \phi^{-c}$ with $a = 0.48 \pm 0.01$, $b = 0.46 \pm 0.02$, and $c = 0.52 \pm 0.01$. (e) Nondimensionalized sorting rate $(k_D\bar{T})^{-1}$ as a function of the aggregation coefficient g and of the nondimensionalized incoming flux ϕ/k_D. At fixed ϕ, faster distillation takes place for intermediate values of g, thus showing the existence of a region of parameter space where sorting is optimal. In this qualitative phase diagram, A, C are high-density phases, characterized by molecule crowding and domain crowding, respectively; B is a low-density phase where the average domain size is much less than the average interdomain separation and sorting domains coexist with freely-diffusing molecules. The dashed line marks maximal sorting at fixed flux ϕ, and divides the B region into regions of less (B_1) and more dilute gas (B_2). Model parameters compatible with experimental values of molecule density and flux are shown as a shaded area.

analysis to a thin layer of approximately 100 nm from the plasma membrane [35]. In these experimental conditions it was possible to observe a large number of endocytic events including the formation and detachment of LDL-enriched vesicles (Fig. 2(b,c)). Growing fluorescently-tagged domains were identified by automated image analysis. Assuming that LDL particles are distributed with approximately constant, uniform probability on the surface of sorting domains, and neglecting curvature corrections, the cumulative fluorescence intensity collected from a given domain is expected to be approximately proportional, in average, to the area of the domain. In order to fix the conversion factor, we assumed that the typical fluorescence intensity reached by growing domains just before their extraction corresponds to the size of mature endocytic vesicles, $R_E \sim 100\,\text{nm}$ [17] (see SM). Histograms of domain sizes (Fig. 2(d)) show an approximately linear dependence of the frequency density on domain size for radii $R < R_E$, compatibly with the behavior predicted by Eq. (4). Assuming $\gamma(R) = 0$ for $R < R_E$ and $\gamma(R) = \gamma_0$ for $R > R_E$, and fitting γ_0, Eq. (4) can be adapted to the experimental data also for $R > R_E$ (Fig. 2(d)).

We measured LDL surface density $\bar{\rho} = 1.7 \cdot 10^{-2}$ ($\sigma_\rho = 0.8 \cdot 10^{-2}$) and flux $\bar{\phi} = 2.8 \cdot 10^{-5}$ ($\sigma_\phi = 1.8 \cdot 10^{-5}$) expressed, respectively, as fraction of the cell surface covered by sorting domains, and fraction of the cell surface extracted per second (see SM), compatibly with previous observations [33]. The microscopic rate k_D can be estimated as D/A_0, where $D = 3 \cdot 10^{-3}\,\mu\text{m}^2/\text{s}$ ($\sigma_D = 1.5 \cdot 10^{-3}\,\mu\text{m}^2/\text{s}$) is the lateral diffusivity of LDL molecules [33, 36], and $A_0 \sim 3 \cdot 10^{-3}\,\mu\text{m}^2$ [37]. The relation $\bar{\phi} = k_I(1 - \bar{\rho}) \simeq k_I$ allows then to estimate $k_I/k_D \sim 10^{-5}$. Fig. 1(a) shows that for such parameter values, experimentally measured densities are attained in the physical model in the vicinity of the minima of the density ρ, i.e in the optimal region. On the phase diagram Fig. 1(e) the g, ϕ pairs compatible with the experiments are found at the intersection of the regions comprised between the numerically computed curves of equation $\rho = \bar{\rho} \pm \sigma_\rho$ and $\phi/k_D = (\bar{\phi} \pm \sigma_\phi)\, A_0\, (D \mp \sigma_D)^{-1}$ (dotted lines in Fig. 1(e)), and are situated in a neighborhood of the optimal region.

Discussion The observation of eukaryotic cells by fluorescence microscopy shows the hectic and apparently chaotic traffic of a myriad of submicrometric vesicles that transport lipids and proteins to disparate subcellular locations [38]. This restless movement takes place at significant energy cost, suggesting that it must be deeply relevant for cell life. Actually, to perform its vital tasks, such as feeding on nutrients, proliferating, migrating, and forming complex multicellular tissues, the cell has first of all to break its original symmetry [39]: in the process, each region of its outer and inner membranes becomes endowed with a specific chemical identity, that allows it to perform its peculiar functions [40]. Vesicular traffic creates and sustains this broken-symmetry state: vesicles enriched in specific molecular factors are continuosly delivered to appropriate membrane regions to maintain their biochemical identity and to contrast the

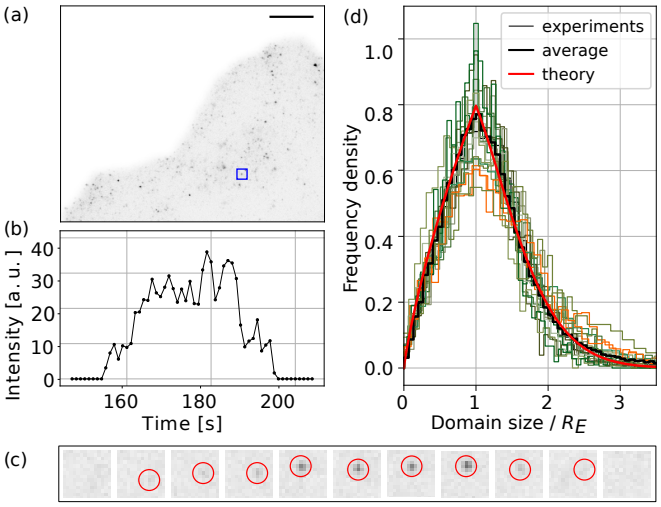

Figure 2. Sorting domains on the cell plasmamembrane. (a) TIRF micrograph of LDL sorting domains; scale bar: 10 µm; blue square: sample region of interest. (b) Time course of fluorescence intensity in the region of interest. (c) Snapshots of the region of interest separated by $\Delta t = 5\,\mathrm{s}$ intervals, starting from $t = 150\,\mathrm{s}$; red circles are centered around an automatically identified growing domain. (d) Frequency density of domain sizes: comparison of a fit of the theoretical curve (4) to data from 18 cells, pooled from two independent experiments. The domain size distribution computed from the complete experimental dataset is represented by the black line. Domain sizes were estimated as described in the text and SM.

homogenizing effect of diffusion [41]. But what are the physical bases of this universal distillation mechanism? We have proposed here a scenario whereby molecular sorting emerges from the coupling of two spontaneous processes: a) phase separation induced by molecular self-aggregation [9, 29, 42], and b) vesicle nucleation. This view has solid bases in the physical chemistry of vesicular traffic, as several mechanisms have been identified that link the formation of molecular aggregates to the induction of membrane bending and vesicle nucleation [15–17, 20, 21, 23]. From this general scenario, the following picture emerges: a continuously repleted gas of molecules diffusing towards multiple sorting centers, that grow due to molecular absorption and lead to the formation of vesicles in which a higher-than-average concentration of the given molecular factor has been distilled. The emergence of an optimal sorting regime at intermediate values of the aggregation strength then follows as a nontrivial effect of the physics of diffusion-limited aggregation on cell membranes, pointing out at the central role of self-aggregation in ordering the system. In our experiments coalescence of domains is rarely observed (see SM), suggesting that domains grow mainly by the absorption of laterally diffusing molecules from the surrounding molecule gas. The opposite regime, where domains mainly grow by coalescence, was considered in Ref. 43. Although here for simplicity we have considered the distillation of a single molecular factor, it is immediately evident that distinct clans of molecules endowed with high intra-clan affinity can separately aggregate in distinct enriched domains and be sorted in parallel. Clans of molecules that participate in common networks of reinforcing catalytic feedback loops are obvious candidates for the spontaneous formation of such enriched domains [9, 29, 42]. By measuring the density of sorting domains and the sorting flux, we observed that LDL endocytosis in primary human endothelial cells kept in steady-state conditions takes place close to the optimal regime. It is then tempting to speculate that an evolutionary constraint may have led the proteins responsible for the distillation process to tune their activity around optimality, as maximal sorting efficiency may have provided selective advantage in terms of faster adaptation to rapidly varying environmental conditions.

MZ, LDA and AG thank Carlo Cosimo Campa, Jean Piero Margaria, Emiliano Descrovi and Emilio Hirsch for useful discussions. Numerical calculations have been made possible through a CINECA-INFN agreement providing access to resources on MARCONI at CINECA. The experimental research described in this manuscript was supported by funding from Fondazione AIRC IG grants #21315 (to GS) and #20366 (to DV).

* Equal contribution.
† guido.serini@ircc.it
‡ kolokol@itp.ac.ru
§ lebede@itp.ac.ru
¶ luca.dallasta@polito.it
** andrea.gamba@polito.it

[1] I. Mellman and W. J. Nelson, Nat. Rev. Mol. Cell Biol. **9**, 833 (2008).
[2] S. Sigismund, S. Confalonieri, A. Ciliberto, S. Polo, G. Scita, and P. P. Di Fiore, Physiol Rev **92**, 273 (2012).
[3] M. M. Kozlov, F. Campelo, N. Liska, L. V. Chernomordik, S. J. Marrink, and H. T. McMahon, Current Opinion in Cell Biology **29**, 53 (2014).
[4] J. H. Hurley, E. Boura, L.-A. Carlson, and B. Różycki, Cell **143**, 875 (2010).
[5] V. Haucke and M. M. Kozlov, J Cell Sci **131** (2018).
[6] M. Mettlen, P.-H. Chen, S. Srinivasan, G. Danuser, and S. L. Schmid, Annual review of biochemistry **87**, 871 (2018).
[7] P. Bassereau, R. Jin, T. Baumgart, M. Deserno, R. Dimova, V. A. Frolov, P. V. Bashkirov, H. Grubmüller, R. Jahn, H. J. Risselada, L. Johannes, M. M. Kozlov, R. Lipowsky, T. J. Pucadyil, W. F. Zeno, J. C. Stachowiak, D. Stamou, A. Breuer, L. Lauritsen, C. Simon, C. Sykes, G. A. Voth, and T. R. Weikl, J Phys D Appl Phys **51** (2018).
[8] L. M. Traub, Biochim Biophys Acta **1744**, 415 (2005).
[9] M. Zamparo, F. Chianale, C. Tebaldi, M. Cosentino-Lagomarsino, M. Nicodemi, and A. Gamba, Soft Matter **11**, 838 (2015).

[10] J. Halatek, F. Brauns, and E. Frey, Philosophical Transactions of the Royal Society B: Biological Sciences **373**, 20170107 (2018).

[11] J. Berry, C. P. Brangwynne, and M. Haataja, Reports on Progress in Physics **81**, 046601 (2018).

[12] A. P. Liu, F. Aguet, G. Danuser, and S. L. Schmid, J Cell Biol **191**, 1381 (2010).

[13] C. Puri, D. Tosoni, R. Comai, A. Rabellino, D. Segat, F. Caneva, P. Luzzi, P. P. Di Fiore, and C. Tacchetti, Molecular Biology of the Cell **16**, 2704 (2005).

[14] P. Sens, L. Johannes, and P. Bassereau, Curr. Opin. Cell Biol. **20**, 476 (2008).

[15] D. J. Busch, J. R. Houser, C. C. Hayden, M. B. Sherman, E. M. Lafer, and J. C. Stachowiak, Nat Commun **6**, 7875 (2015).

[16] J. C. Stachowiak, E. M. Schmid, C. J. Ryan, H. S. Ann, D. Y. Sasaki, M. B. Sherman, P. L. Geissler, D. A. Fletcher, and C. C. Hayden, Nat. Cell Biol. **14**, 944 (2012).

[17] M. Kaksonen and A. Roux, Nat. Rev. Molec. Cell Biol. **19**, 313 (2018).

[18] N. S. Gov, Philosophical Transactions of the Royal Society B: Biological Sciences **373**, 20170115 (2018).

[19] Z. Chen, E. Atefi, and T. Baumgart, Biophys J **111**, 1823 (2016).

[20] S. Leibler, J. de Physique **47**, 507 (1986).

[21] S. Leibler and D. Andelman, J. de Physique **48**, 2013 (1987).

[22] A. F. Bitbol, L. Peliti, and J. B. Fournier, Europ. Phys. J. E **34** (2011).

[23] A. Banerjee, A. Berezhkovskii, and R. Nossal, Biophys. J. **102**, 2725 (2012).

[24] S. A. Rautu, G. Rowlands, and M. S. Turner, Physical Review Letters **114**, 098101 (2015).

[25] L. Foret and P. Sens, Proc. Natl. Acad. Sci. USA **105**, 14763 (2008).

[26] A.-L. Barabasi and H. E. Stanley, Fractal Concepts in Surface Growth (Cambridge University Press, Cambridge, 1995).

[27] H. S. Hele-Shaw, Nature **58**, 34 (1898).

[28] V. V. Slezov, Kinetics of First Order Phase Transitions (Wiley-VCH Verlag GmbH & Co. KGaA, Weinheim, 2009).

[29] A. Gamba, I. Kolokolov, V. Lebedev, and G. Ortenzi, Phys Rev Lett **99**, 158101 (2007).

[30] L. Bertini, A. D. Sole, D. Gabrielli, G. Jona-Lasinio, and C. Landim, J. Stat. Mech.: Theory and Experiment **2007**, P07014 (2007).

[31] M. Zamparo, L. Dall'Asta, and A. Gamba, J. Stat. Phys. **174**, 120 (2019).

[32] Since ϕ is a monotonically increasing function of the insertion rate k_I (see SM), by a change of variable ϕ (which is directly observable) can be used as a control parameter in the place of k_I (which is not observable).

[33] B. Goldstein, C. Wofsy, and G. Bell, Proc. Natl. Acad. Sci. USA **78**, 5695 (1981).

[34] G. Mana, F. Clapero, E. Panieri, V. Panero, R. T. Böttcher, H.-Y. Tseng, F. Saltarin, E. Astanina, K. I. Wolanska, M. R. Morgan, M. Humphries, M. Santoro, G. Serini, and D. Valdembri, Nat. Commun. **7**, 13546 (2016).

[35] A. Picco and M. Kaksonen, Curr. Opin. Cell Biol. **53**, 105 (2018).

[36] L. S. Barak and W. W. Webb, J. Cell Biol. **95**, 846 (1982).

[37] Single molecule measurements show that endocytic vesicles host $\pi R_E^2/A_0 \sim 10$ LDL molecules [44].

[38] B. Sönnichsen, S. De Renzis, E. Nielsen, J. Rietdorf, and M. Zerial, J. Cell Biol. **149**, 901 (2000).

[39] R. Wedlich-Söldner and R. Li, Nat. Cell Biol. , 267 (2003).

[40] E. Rodriguez-Boulan and I. G. Macara, Nat. Rev. Molec. Cell Biol. **15**, 225 (2014).

[41] A. Shewan, D. J. Eastburn, and K. Mostov, Cold Spring Harb. Perspect. Biol. , a004796 (2011).

[42] A. Gamba, A. de Candia, S. Di Talia, A. Coniglio, F. Bussolino, and G. Serini, Proc. Natl. Acad. Sci. USA **102**, 16927 (2005).

[43] S. Heinzer, S. Worz, C. Kalla, K. Rohr, and M. Weiss, J. Cell Sci. **121**, 55 (2008).

[44] R. G. Anderson, M. S. Brown, and J. L. Goldstein, Cell **10**, 351 (1977).

Optimality in self-organized molecular sorting – Supplemental Material

Marco Zamparo, Donatella Valdembri, Guido Serini, Igor V. Kolokolov,
Vladimir V. Lebedev, Luca Dall'Asta, and Andrea Gamba

A. Lattice-gas model

The computational model is defined on a periodic square lattice containing L^2 sites. The presence/absence of a molecule on site i is denoted by the binary variable η_i. The kinetics of distillation is described by the continuous-time Markov process specified by the infinitesimal generator $\mathcal{L} = \mathcal{L}_I + \mathcal{L}_D + \mathcal{L}_E$, whose components are the generators for molecule insertion, diffusion-aggregation, and extraction, defined as follows. We recall here that if $f(\eta)$ is a function of the state $\eta = \{\eta_i\}$, the generator $\mathcal{L}$ of the process is the operator defined by the relation $\partial_t \overline{f(\eta)} = \overline{\mathcal{L} f(\eta)}$, where the average is over the realizations of the stochastic process [1, 2].

Allowed moves are (see also scheme in Fig. 1):

Insertion – Molecules are inserted at empty sites with insertion rate k_I:

$$\mathcal{L}_I f(\eta) = k_I \sum_i (1-\eta_i)[f(\eta^i) - f(\eta)]$$

where the configuration η^i differs from η only for the insertion of a molecule on site i.

Diffusion and aggregation – Molecules can jump on empty neighboring sites:

$$\mathcal{L}_D f(\eta) = k_D \sum_i \sum_{j \in N_i} \eta_i (1-\eta_j) g_i(\eta) [f(\eta^{ij}) - f(\eta)]$$

where N_i are the nearest neighbors of i, the configuration η^{ij} differs from η only for the jump of a molecule from i to j, and the factor

$$g_i(\eta) = \prod_{k \in N_i} g^{-\eta_k}$$

reduces the probability of jumps that break links with neighboring occupied sites. High values of the aggregation coefficient $g \geqslant 1$ favor the formation of molecular aggregates.

Extraction – Connected components containing at least a square region V of linear size ℓ completely filled with molecules are extracted with rate k_E:

$$\mathcal{L}_E f(\eta) = k_E \sum_{C \in \mathscr{C}} h\Big(\sum_{V \subset C} \prod_{j \in V} \eta_j \Big) [f(\eta^C) - f(\eta)]$$

where $\mathscr{C}$ is the collection of connected subsets of the lattice, $h(x) = 0$ for $x = 0$, $h(x) = 1$ for $x > 0$, V is a square region of linear size ℓ, and the configuration η^C is obtained from η by emptying all of the sites in C. Simulations were performed in the limit $k_E \to \infty$ with $L = 400$ and $\ell = 3$ using Gillespie's algorithm [3].

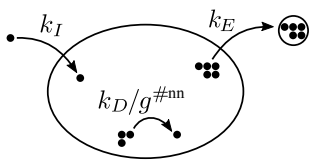

Figure 1. Minimal model for molecular sorting.

B. Residence time

The average number of molecules inserted into the membrane system per site and per unit time is

$$\phi = k_I (1 - \rho)$$

since molecules can only be inserted at empty sites. Areas are measured here in units of a lattice site. In the statistically stationary state, ϕ coincides with the flux of extracted molecules. Since there can be at most a single molecule per site, ϕ can also be interpreted as the fraction of membrane area extracted from the system per unit time. Numerical simulations of the statistically stationary state show that ϕ is a monotonically increasing function of k_I at fixed g (Fig. 2).

Let the residence time T spent by a molecule on the membrane system in the statistically stationary state be a stochastic variable with probability density $p(t)$. The average number ρ of particles per site that are found on the membrane system at time $t = 0$ is the sum of the $\phi\,\mathrm{d}t$ particles introduced in average during previous time intervals of duration $\mathrm{d}t$, such that their permanence time has not yet elapsed:

$$\rho = \int_0^\infty \mathrm{Prob}(T > t)\, \phi\, \mathrm{d}t \;=\; \phi \int_0^\infty \Big(\int_t^\infty p(\tau)\, \mathrm{d}\tau \Big) \mathrm{d}t$$
$$= \phi \int_0^\infty \tau\, p(\tau)\, \mathrm{d}\tau \;=\; \phi\, \overline{T}$$

The average residence time of a molecule in the system is therefore $\overline{T} = \rho/\phi$. This exact relation holds for a large class of stochastic lattice-gas models with general injection, diffusion and extraction dynamics [4].

C. Adaptation time

The main timescale characterizing the behavior of the stationary state of the system is the residence time $\bar{T}$.

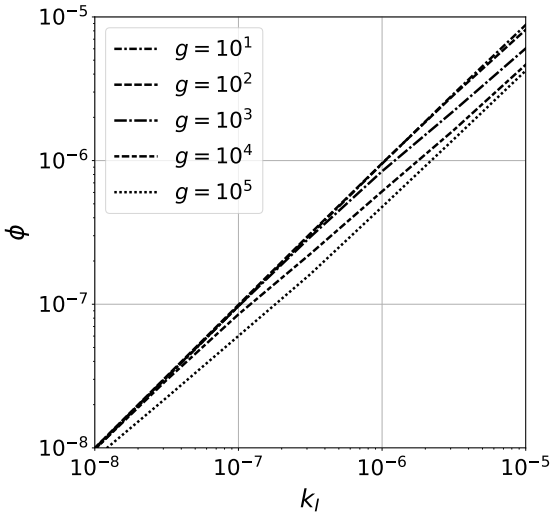

Figure 2. Monotonic dependence of the molecule flux ϕ on the insertion rate k_I at fixed values of the aggregation coefficient g, in the statistically stationary state.

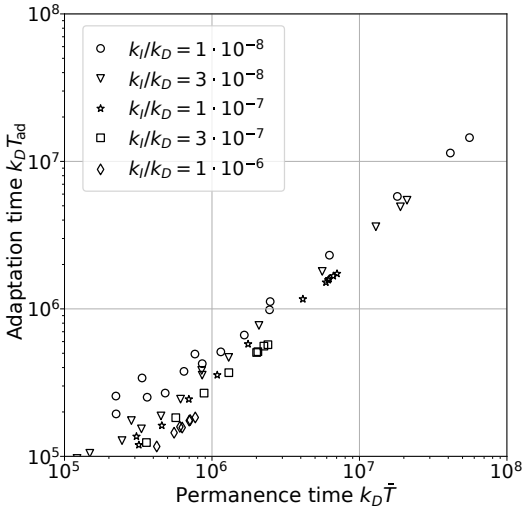

Figure 3. Direct correlation of the nondimensionalized residence time $k_D\,\bar{T}$ and adaptation time $k_D\,T_{\rm ad}$.

But there is a second relevant timescale: the characteristic adaptation time $T_{\rm ad}$ needed by the membrane system to approach the stationary state after the sudden onset of a nonzero external stimulus. The time $T_{\rm ad}$ can be seen as the time needed by the cell to adapt to a sudden variation in extracellular conditions, and has therefore direct biological relevance. The adaptation time $T_{\rm ad}$ was computed numerically by preparing the system with $\rho = 0$ at time $t = 0$, switching on a constant $k_I > 0$ for $t > 0$ to mimick the sudden onset of an extracellular signal, and fitting the obtained time-dependent density profile $\rho(t)$ with an exponential function. The measure was repeated for several different values of g and ϕ_0. By plotting the resulting values of the adaptation time $T_{\rm ad}$ against the residence time $\bar{T}$ it is seen that the two timescales are directly correlated (Fig. 3). Therefore, parameter values that correspond to optimal sorting in the stationary state are also expected to provide faster transient response to changing environmental signals.

D. Experimental system

LDL endocytosis has been thoroughly studied for its fundamental role in the removal of highly atherogenic LDL particles from the circulation [5]. Low-density lipoproteins (LDL) bind to LDL receptors (LDLR) on the plasma membrane, diffuse laterally, aggregate and are internalized in endocytic vesicles [6, 7]. Binding of LDL to LDLR takes place with a 1:1 stoichiometry, as each LDL particle contains a single APOB100 protein that binds to the single LDL-binding site (site B) of an LDLR with high affinity [8–10]. The resulting receptor-ligand complex diffuses on the plasmamembrane and aggregates in domains that are subsequently endocyted [6, 11]. This complex biophysical process is described in abstract terms in our physical model as the random insertion of an LDL particle in the plasmamembrane with rate k_I, its subsequent diffusion with diffusivity D, aggregation in an LDL-enriched domain, and ultimate extraction of the domain.

E. Cell culture

Primary arterial endothelial cells (AECs) were isolated from umbilical cords as previously described [12] and grown in Endothelial Cell Growth Basal Medium (EBM-2) supplemented with EGM-2 BulletKit (Lonza Basel, Switzerland) (EGM-2). The isolation of primary arterial ECs human umbilical cords was approved by the Office of the General Director and Ethics Committee of the Azienda Sanitaria Ospedaliera Ordine Mauriziano di Torino hospital (protocol approval no. 586, Oct 22 2012 and no. 26884, Aug 28 2014) and informed consent was obtained from each patient. AECs were serum starved for 3 hours. Then, AECs were incubated with $4\,\mu g/$ml acetylated Low Density Lipoprotein from human plasma, Alexa Fluor 488 Conjugated (Thermo Fisher Scientific, Waltham, MA USA) for 1 hour to allow reaching a steady state before starting imaging.

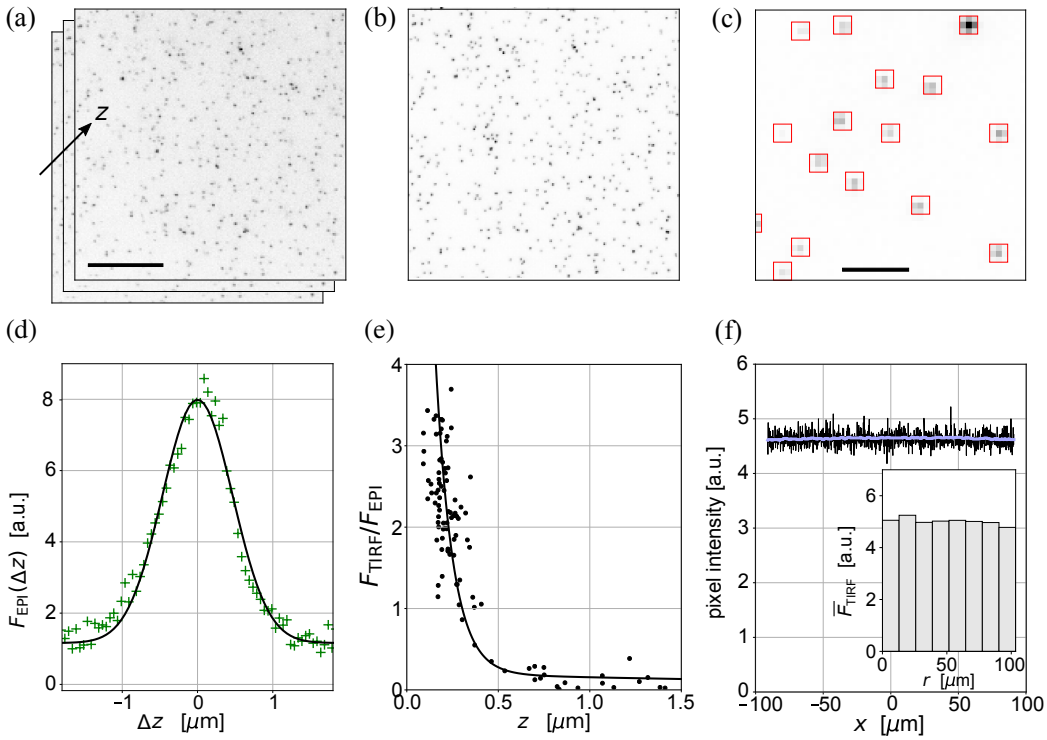

Figure 4. Determining the TIRF penetration depth and the degree of evenness of illumination. (a) A z-stack of images of 100 nm fluorescent beads dispersed in transparent agarose gel was acquired in epifluorescence (bar=10 µm). (b) The beads were also imaged in TIRF. (c) Automatical identification of the TIRF images of fluorescent beads (bar=2 µm). (d) The z location of each bead was determined by a Gaussian fit of its axial fluorescence profile $F_{EPI}(z)$. (e) The penetration depth of the evanescent wave was found by fitting the normalized TIRF fluorescence F_{TIRF}/F_{EPI} for each bead with the theoretical decay curve [13]. (f) Typical intensity profile observed by imaging a solution of Alexa Fluor 488 (black line), and the same after local Gaussian smoothing (light blue). Inset: radial frequency distribution of the mean intensity of beads fluorescence.

F. Time-lapse TIRF microscopy

TIRF microscopy on living ECs was performed using a Leica AM TIRF MC system mounted on a Leica AF 6000LX workstation. Cells were plated onto glass-bottom dishes (WillCo-dish; Willcowells, Amsterdam, The Netherlands) coated with 3 µg/ml human plasma fibronectin (1918-FN-02M, R&D, Systems, Minneapolis, MN, USA) and placed onto a sample stage within an incubator chamber set to 37°C, in an atmosphere of 5% CO_2, 20% humidity. A Leica HC PL APO 63×/1.47 NA oil-immersion objective was used, and laser penetration depth was set at 90 nm (see below). Excitation and analysis of fluorescent proteins were performed with a 488 nm laser. Imaging was recorded on a Hamamatsu EM-CCD camera (C9100-02, Hamamatsu, SZK, Japan).

G. TIRF calibration

In TIRF microscopy, light is directed toward the glass/water (or glass/specimen) interface with a large incidence angle. At the interface of the two transparent media light is totally reflected, and only an evanescent (exponentially decaying) electromagnetic field penetrates beyond the interface. This way, only fluorophores within a thin section at the bottom of the cells are excited, thereby excluding most of the cellular background fluorescence [14]. In the TIRF system used, data from an integrated sensor is elaborated by the system software to adjust the incidence angle so that the penetration depth of the evanescent field is set to the desired value. In order to focus at the closest possible distance from the plasma membrane, a penetration depth of 90 nm was selected. To ensure reproducibility, the penetration depth of the evanescent wave was independently measured following the protocol exposed in detail in Ref. 13, which is briefly summarized in the following paragraph.

A solution of 0.1 µm diameter Tetraspeck Microspheres (Invitrogen) diluted 1:4 in distilled water was pipetted in small droplets of 1 µl on the glass bottom of a WillCo-dish (WillCo Wells) and left to dry. Adherent microspheres were covered with 20 µl of a solution containing of 0.5% low-melting-point agarose solu-

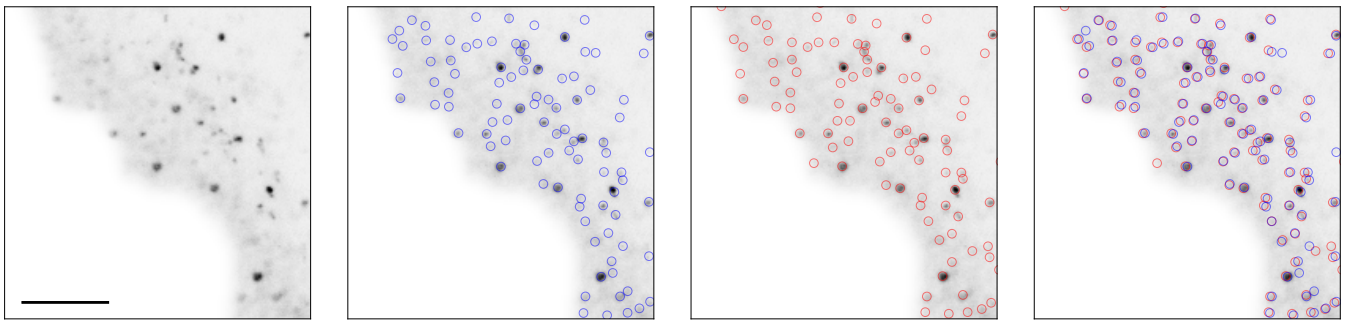

(a) (b) (c) (d)

Figure 5. Automatic recognition of endocytic domains (scalebar: 10 µm). (a) enlarged TIRF image of LDL fluorescent domains; (b) domains identified by visual inspection (95 blue circles); (c) automatically recognized domains (94 red circles); (d) comparison between visual and automatic domain recognition (5 false positives, 6 false negatives);

tion (SeaPlaque), 842 mM sucrose and Tetraspeck Microspheres diluted 1:3. The agarose was allowed to polymerize and then 2 ml of agarose/sucrose solution (not containing microspheres) was slowly deposited on top of it. Images of the beads were acquired in epifluorescence (EPI) focusing at increasing distances z from the reflecting interface (Fig. 4a). The beads were also imaged in TIRF in the same conditions as the specimens of interest (Fig. 4b). The images of the beads were automatically identified by a standard blob detection algorithm (see following Section for details), the (x, y) coordinates of their centers were determined, and a mean intensity F was computed by averaging the intensities of a set of 3×3 pixels centered in (x, y) (Fig. 4c, red squares). The same procedure was applied to EPI images for each given distance z from the reflecting surface, thus deriving an axial fluorescence profile $F_{\mathrm{EPI}}(z)$ for each bead. The distance z of each bead from the reflecting interface was determined from the position of the peak of the Gaussian profile that best fitted $F_{\mathrm{EPI}}(z)$ (Fig. 4d). By finally fitting the normalized TIRF fluorescence $F_{\mathrm{TIRF}}/F_{\mathrm{EPI}}$ for each bead with the theoretical decay curve [13] (Fig. 4e) a TIRF penetration depth of 93 ± 20 nm was found.

The degree of evenness of TIRF illumination across the field of view [15, 16] was checked by two different methods. First, 1 ml of a solution 6.6 µM of phalloidin Alexa488 conjugated was pipetted on a WillCo-dish and imaged in TIRF under the same conditions as the specimens of interest [15, 17], obtaining a matrix I_{ij} of values of pixel intensities (a typical intensity profile along the x axis is shown in Fig. 4f, black line). To average out local fluctuations that are not related to unevenness of illumination at the scale of the field of view, the matrix I_{ij} was convolved with a Gaussian kernel of 5 pixel aperture to obtain a smoothed image I^{s}_{ij} (a typical smoothed profile is shown in Fig. 4f, light blue). The maximum relative deviation from the mean, computed over the whole area of the smoothed image as $\max_{ij}(I^{\mathrm{s}}_{ij}/\overline{I^{\mathrm{s}}} - 1)$, was less then 3%. Secondly, the TIRF images of the same fluorescent beads previously used to measure the penetration length of the TIRF evanescent wave were analyzed in the following way. The mean TIRF signal $\overline{F}_{\mathrm{TIRF}}$ from each bead was considered as a function of the distance r from the center of the field of view, and a frequency histogram was computed (Fig. 4f, inset). The obtained frequency distribution differed by a flat distribution again by less than 3%. Overall, this showed that applying a correction for the unevenness of illumination would not significantly improve the precision of our experimental results.

H. Image processing

Photograms from 18 movies obtained by two indipendent experiments, of approximately 200 s duration, separated by 1 s time intervals were analyzed using the open-source software SciPy (scipy.org) and OpenCV (opencv.org). A binary mask was used to isolate single cells from images containing more than one cell. Fluorescent circular domains were identified using the standard blob detection algorithm based on the Laplacian of the Gaussian method [18]. In this algorithm, the only relevant free parameter was the number N_{b} of recognized blobs, which the algorithm lists in order of decreasing values of a score function [18]. Fig. 5 provides a qualitative assessment of the efficacy of the blob detection algorithm in the current problem. Domains from the micrograph in Fig. 5(a) were identified by visual inspection (Fig. 5(b)). Setting $N_{\mathrm{b}} \sim 1000$ in the algorithm the domains shown in Fig. 5(c) were automatically detected. The comparison in Fig. 5(d) shows that the automatic identification of domains performed by the algorithm is compatible with the identification performed by a human operator. Starting from this qualitative assessment, we investigated the dependence of the size distribution of the automatically identified sorting domains

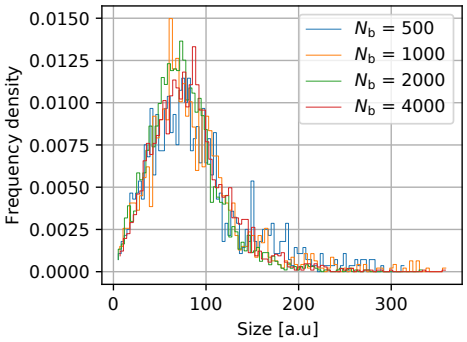

Figure 6. The domain size distribution is stable with respect to variations of the number N_b of automatically identified LDL domains.

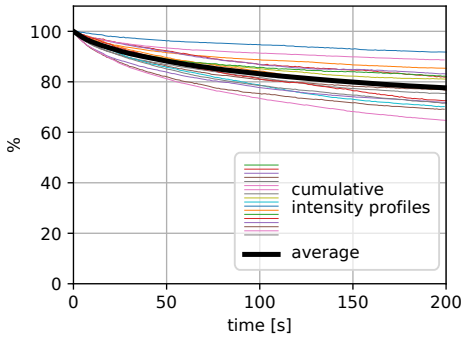

Figure 7. Normalized photobleaching curves.

on N_b. The size distribution was analyzed for domains with lifetime $> 5\,s$ in order to neglect the short, time-uncorrelated fluctuations that the algorithm is able to identify for high values of N_b, but that do not evolve into steadily growing domains. As a consequence, the resulting shape of the size distribution turned out to be remarkably robust with respect to variations of N_b over a wide range of values (Fig. 6). This range of values was the same for all the movies analyzed, as they were acquired with the same protocol. Background fluorescence intensity was computed as the average of the fluorescence intensity of pixels outside of circular domains. Domains whose images overlapped in two subsequent photograms were identified and their centers computed. Net fluorescence intensity values $I_{f,p}$ were collected from each frame f and pixel p after background subtraction. For each domain d, the cumulative fluorescence intensity was computed as $I_{d,f} = \sum_{p \in C_{f,d}} I_{f,p}$, with $C_{f,d}$ the circle of radius 500 nm centered on domain d. A peak value I_E was derived from the histogram of the square root of fluorescence intensities, and the value $I_d = \max_f (I_{d,f})$ was computed for each domain d. Experimental estimates of the fraction ρ of membrane area covered by sorting domains, and the fraction ϕ of membrane area extracted per photogram (and therefore per second) were computed as

$$\rho = \frac{1}{M} \sum_f \sum_d \frac{I_{d,f}}{I_E} \frac{A_E}{A} \tag{1}$$

$$\phi = \frac{1}{M} \sum_{I_d > I_E} \frac{I_d}{I_E} \frac{A_E}{A} \tag{2}$$

where $A_E = \pi R_E^2$ is the area of membrane extracted during an endocytic event, A is the area of the cell membrane observed in the experiment, and M is the number of photograms. The dimensionless density ρ and the dimensionless ratio ϕ/k_D were used in the comparison with numerical simulations.

I. Photobleaching

To assess the effect of photobleaching we measured the cumulative fluorescence of single photograms from experimental data (18 movies of 200 s duration, 1 photogram/s acquisition rate) following the procedure described in Ref. 15 (Sect. 5.4.1). Photobleaching curves (Fig. 7) show in average a 20% decrease in fluorescence between the first and last frame. Densities and fluxes were computed after correcting for photobleaching [15, Secs. 1.6.3, 5.4.1]. We found that the variation between the values of densities and fluxes computed with and without the correction was within the measurement errors, that were estimated by computing standard deviations. Values have therefore been reported in the main text without correcting for photobleaching, in order to avoid introducing artifacts and arbitrary choices, as there is not a unique way to correct for photobleaching, and part of the decrease in the observed fluorescence may be due to the endocytic process itself.

J. Fluctuations

The growth of sorting domains is an intrinsically stochastic process. Observation of domain growth by fluorescence microscopy introduces further layers of stochasticity, related to the varying number of fluorophores hosted by a given cargo molecule, the varying number of photons emitted by a given fluorophore, etc. [15]. The number of fluorophores on a domain of size R can be modeled as a Poisson random variable of mean $(R/R_E)^2\, n_m\, n_f$, where n_m is the average number of cargo molecules contained in a domain of size R_E, and n_f is the average number of fluorophores per cargo molecule. To estimate the effect of stochastic fluctuations on experimental observations of domain growth by fluorescence microscopy, a virtual experimental observation was simulated by randomly sampling 2500 domain sizes from the theoretical probability distibution (Main Text, Eq. 4).

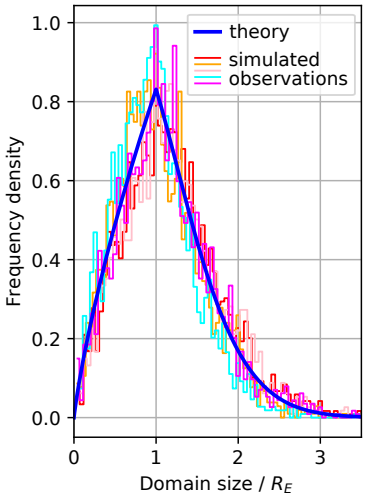

Figure 8. Simulated observations of domain sizes. For each simulated observation, 2500 domain sizes were randomly sampled from the theoretical distribution (blue curve). The number of fluorophores per cargo molecule were modeled as Poisson random variables.

For each domain size R a number of fluorophores was then extracted from the corresponding Poisson distribution, with $n_{\rm m} = 10$, $n_{\rm f} = 32$. The resulting simulated observations show fluctuations around the theoretical probability distribution (Fig. 8) similar to those observed in actual experiments (Fig. 2d, Main Text). Taking into account also the stochastic fluctuations due to the variable number of photons emitted per fluorophore one gets results that are indistinguishable from those shown in Fig. 8, due to the law of large numbers [19] and the high number of photons emitted per fluorophore, which is of the order of 10^3 [20].

The combined effect of the statistical fluctuations in both the number $n_{\rm f}$ of fluorophores and in the number $n_{\rm ph}$ of photons emitted per fluorophore per unit time can be estimated analytically if the two random variables are assumed to be Poisson distributed:

$$P_{\rm f}(m) = \frac{n_{\rm f}^m}{m!}{\rm e}^{-n_{\rm f}} \tag{3}$$

$$P_{\rm ph}(n) = \frac{n_{\rm ph}^n}{n!}{\rm e}^{-n_{\rm ph}} \tag{4}$$

The probability that q photons are emitted in total in a given time interval can be obtained by the following double average:

$$P_{\rm tot}(q) = \langle\langle \Delta(q - n_1 - n_2 - \ldots - n_N)\rangle_{\rm ph}\rangle_{\rm f} \tag{5}$$

where $\Delta(m)$ is the discrete delta-function:

$$\Delta(m) = 0, \quad m \neq 0, \quad \Delta(0) = 0$$

which has the integral representation:

$$\Delta(m) \quad = \quad \frac{1}{2\pi}\int_0^{2\pi} {\rm d}\theta\, {\rm e}^{i\,m\,\theta} \tag{6}$$

The first average in (5) is with respect to the set of numbers $n_1, n_2, \ldots, n_N$, each distributed as (4), the second average is over the distribution (3), and gives:

$$P_{\rm tot}(q) = \frac{1}{2\pi}\int_0^{2\pi} {\rm d}\theta\, {\rm e}^{i\,q\,\theta}{\rm e}^{-n_{\rm f}} \times \tag{7}$$

$$\times \sum_{m=0}^{\infty} \frac{n_{\rm f}^m}{m!}{\rm e}^{-m n_{\rm ph}} \left(\sum_{n=0}^{\infty} \frac{n_{\rm ph}^n {\rm e}^{-i\,n\,\theta}}{n!}\right)^m =$$

$$= \frac{1}{2\pi}\int_0^{2\pi} {\rm d}\theta\, {\rm e}^{i\,q\theta - n_{\rm f}[1-{\rm e}^{-n_{\rm ph}(1-{\rm e}^{-i\,\theta})}]} \tag{8}$$

This exact integral representation of the distribution of interest results from averaging over two Poisson distributions, but it is not their simple convolution. However, if $n_{\rm ph}, n_{\rm f} \gg 1$ the integration can be performed by the saddle-point method, obtaining:

$$P_{\rm tot}(q) \propto \frac{1}{\sqrt{q n_{\rm ph}^2}} \exp\left[-\frac{q}{n_{\rm ph}} \ln\left(\frac{q}{n_{\rm f} n_{\rm ph} e}\right) - n_{\rm f}\right] \tag{9}$$

which is sharply peaked at $q = n_{\rm ph} n_{\rm f}$, and well approximated by the Gaussian distribution:

$$P_{\rm tot}(q) \approx \frac{1}{\sqrt{2\pi n_{\rm f} n_{\rm ph}^2}} \exp\left[-\frac{n_{\rm f}}{2}\left(\frac{q}{n_{\rm f} n_{\rm ph}} - 1\right)^2\right] \tag{10}$$

which has mean value $n_{\rm tot} = n_{\rm f} n_{\rm ph}$ and standard deviation $\sigma = \sqrt{n_{\rm f} n_{\rm ph}^2}$.

K. Estimation of domain areas

Assuming that fluorescent cargo molecules are distributed with approximately constant, uniform probability on the surface of sorting domains, the cumulative fluorescence intensity collected from a given domain is proportional, in average, to the number of fluorescent cargo molecules in the domain, and, again in average, to the area of the domain, the conversion factor being the average surface concentration of cargo molecules in sorting domains. In order to fix this conversion factor, we assumed that the typical fluorescence intensity reached by growing domains just before their extraction corresponds to the size of mature endocytic vesicles, $R_E \sim 100\,{\rm nm}$ [21] (see Eqs. 1, 2). Stochastic deviations around the average are expected to produce fluctuations in the observational curves similar to those shown in Fig. 8.

In mammalian cells, clathrin-mediated endocytosis has been observed to pass through an initial growth regime

during which growing domains are approximately planar, and a final invagination stage during which the curvature of domains increases until a new vesicle is formed [22]. During the invagination stage the shape of sorting domains changes progressively from approximately circular to approximately spherical [14], with consequent changes of the ratios between the area, perimeter, and linear size of the domain [23]. These geometric effects can be neglected in a first approximation when computing diffusive fluxes, since the flux of molecules toward a domain has only a weak logarithmic dependence on its linear size (see Eq. (2), Main Text). When analyzing TIRF data, the effect of rounding of the fluorescent domain during the invagination stage can be estimated by means of the following ideal model. Taking into account the decay of the TIRF evanescent wave, the fluorescence emitted by a uniform distribution of fluorophores over a sherical dome of radius $r = c^{-1}$ and area A in contact with the coverglass plane along its circular border is proportional to $I(c) = 2\pi r^2 \int_0^{\theta_0} \sin\theta \, \mathrm{d}\theta \, \mathrm{e}^{-\frac{r}{\lambda}(\cos\theta - \cos\theta_0)}$, where λ is the laser penetration depth and θ_0 is the angle formed by the spherical dome with the coverglass plane. From this formula, the curvature correction $\frac{I(c)}{I(0)} = \frac{2\pi\lambda}{cA}(1 - \mathrm{e}^{-\frac{cA}{2\pi\lambda}})$ can be derived. Assuming a uniform increase in curvature during the invagination process that leads to the formation of a spherical vesicle of area $A_E = 4\pi(R_E/2)^2$ with $R_E/2 = 50\,\mathrm{nm}$, this gives $\overline{I(c)} = 0.797 \cdot I(0)$, i.e. an average correction of the order of 20% in the estimation of the domain area, corresponding to a 10% correction in the estimation of the linear domain size, during the invagination stage. We chose to not apply this correction to our data, as it is model-dependent and of the order of the experimental uncertainty.

As a further characterization of the experimental system, we imaged the distribution of fluorescence intensities coming from single LDL particles immobilized on a coverslip. To this effect, a solution of *** [aggiungere concentrazione... qui bisogna ripetere proprio tutto come in sez. G? ho riportato quanto scritto per le sferette, c'é qualcosa da cambiare?] *** acetylated Low Density Lipoprotein from human plasma, Alexa Fluor 488 Conjugated (Thermo Fisher Scientific, Waltham, MA USA) was pipetted in small droplets of 1 µl on the glass bottom of a WillCo-dish (WillCo Wells) and left to dry. Deposited LDL particles were immobilized by adding 2 ml of a solution containing 0.5% low-melting-point agarose solution (SeaPlaque) and 842 mM sucrose that was then allowed to polymerize. TIRF images of control LDL particles on coverslip were acquired and their fluorescence intensities measured using the procedure previously applied to Tetraspeck Microspheres (see Section G and Fig. 9(a,b)). In Fig. 9(c,d) the distribution of the fluorescence intensities of control LDL particles on coverslip (magenta) is compared to that of experimental LDL sorting domains in live cells (red), while Fig. 9(e,f) show the corresponding distributions of the square roots of fluorescence intensities.

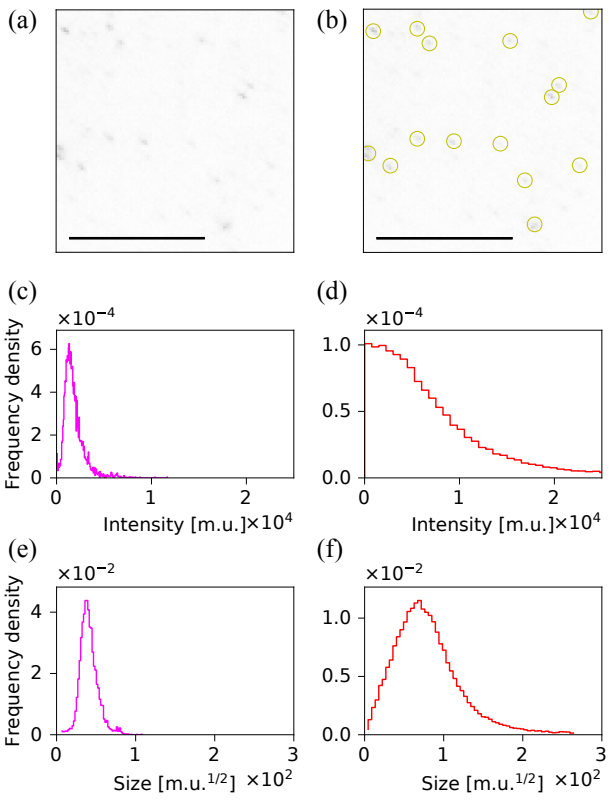

Figure 9. (a) TIRF image of control LDL particles on coverslip; (b) automatic identification of control LDL particles from the image in (a) (red circles; scalebar: 10 µm in both panels). Histograms: (c,d) fluorescence intensities of control LDL particles on coverslip (magenta) and of experimental LDL sorting domains on live cells (red); (e,f) square roots of intensities of control LDL particles on coverslip (magenta) and experimental LDL sorting domains on live cells (red).

L. Domain mobility

Aggregation phenomena have been described through theoretical models belonging to different universality classes [24], including models where aggregation is driven by individual diffusing particles [25] and models governed by domain coalescence [26]. Domain coalescence is expected to dominate when domains are highly mobile and have a high probability of encounter. In our experiments, the average distance between neighboring domain was 2.0 µm ($\sigma = 1.5$ µm), while the average displacement of cluster centroids during observation time was 0.15 µm ($\sigma = 0.19$ µm) i.e. one order of magnitude less. Coherently with these data, only 0.5% of domain trajectories were observed to coalesce, suggesting that domains grow mainly by the absorption of laterally diffusing molecules

from the surrounding molecule gas.

[1] J. Marro and R. Dickman, *Nonequilibrium Phase Transitions in Lattice Models (Collection Alea-Saclay: Monographs and Texts in Statistical Physics)* (Cambridge University Press, 2005).

[2] L. Bertini, A. D. Sole, D. Gabrielli, G. Jona-Lasinio, and C. Landim, J. Stat. Mech.: Theory and Experiment **2007**, P07014 (2007).

[3] D. T. Gillespie, J. Comput. Phys. **22**, 403 (1976).

[4] M. Zamparo, L. Dall'Asta, and A. Gamba, J. Stat. Phys. **174**, 120 (2019).

[5] M. S. Brown, J. L. Goldstein, *et al.*, Science **232**, 34 (1986).

[6] B. Goldstein, C. Wofsy, and G. Bell, Proc. Natl. Acad. Sci. USA **78**, 5695 (1981).

[7] I. Mellman and W. J. Nelson, Nat. Rev. Mol. Cell Biol. **9**, 833 (2008).

[8] T. Hevonoja, M. O. Pentikäinen, M. T. Hyvönen, P. T. Kovanen, and M. Ala-Korpela, Biochimica et Biophysica Acta (BBA) - Molecular and Cell Biology of Lipids **1488**, 189 (2000).

[9] W. J. Schneider, in *Biochemistry of Lipids, Lipoproteins and Membranes (Sixth Edition)*, edited by N. D. Ridgway and R. S. McLeod (Elsevier, 2016) sixth edition ed., pp. 489 – 518.

[10] T. L. Innerarity, R. E. Pitas, and R. W. Mahley, in *Plasma Lipoproteins Part B: Characterization, Cell Biology, and Metabolism*, Methods in Enzymology, Vol. 129 (Academic Press, 1986) pp. 542 – 565.

[11] M. Ehrlich, W. Boll, A. Van Oijen, R. Hariharan, K. Chandran, M. L. Nibert, and T. Kirchhausen, Cell **118**, 591 (2004).

[12] G. Mana, F. Clapero, E. Panieri, V. Panero, R. T. Böttcher, H.-Y. Tseng, F. Saltarin, E. Astanina, K. I. Wolanska, M. R. Morgan, M. Humphries, M. Santoro, G. Serini, and D. Valdembri, Nat. Commun. **7**, 13546 (2016).

[13] M. Oheim, A. Salomon, A. Weissman, M. Brunstein, and U. Becherer, Biophysical Journal **117**, 795 (2019).

[14] A. Picco and M. Kaksonen, Curr. Opin. Cell Biol. **53**, 105 (2018).

[15] J. C. Waters and T. W. (Eds.), *Quantitative Imaging in Cell Biology*, 1st ed., Methods in Cell Biology Volume 123 (Academic Press, 2014).

[16] I. Khaw, B. Croop, J. Tang, A. Möhl, U. Fuchs, and K. Y. Han, Optics Express **26**, 15276 (2018).

[17] M. A. Model, Current Protocols in Cytometry **37**, 10.14.1 (2006).

[18] T. Lindeberg, International journal of computer vision **30**, 79 (1998).

[19] F. Dekking, C. Kraaikamp, H. Lopuhaä, and L. Meester, *A Modern Introduction to Probability and Statistics: Understanding why and how* (Springer, 2007).

[20] G. T. Dempsey, J. C. Vaughan, K. H. Chen, M. Bates, and X. Zhuang, Nature methods **8**, 1027 (2011).

[21] M. Kaksonen and A. Roux, Nat. Rev. Molec. Cell Biol. **19**, 313 (2018).

[22] O. Avinoam, M. Schorb, C. J. Beese, J. A. G. Briggs, and M. Kaksonen, Science **348**, 1369 (2015).

[23] The area of a planar domain was defined in the Main Text as $A=\pi R^2$, therefore R can be identified with the diameter $2R$ of a spherical vesicle having the same area A.

[24] M. Kolb, R. Botet, and R. Jullien, Physical Review Letters **51**, 1123 (1983).

[25] T. A. Witten and L. M. Sander, Phys. Rev. Lett. **47**, 1400 (1981).

[26] P. Meakin, Physical Review Letters **51**, 1119 (1983).